


RESEARCH ARTICLE

Open Access



An intimate view into the silica deposition vesicles of diatoms

Christoph Heintze¹, Petr Formanek⁴, Darius Pohl⁵, Jannes Hauptstein¹, Bernd Rellinghaus⁵ and Nils Kröger^{1,2,3*} 

Abstract

Diatoms are single-celled microalgae that produce silica-based cell walls with intricate nano- and micropatterns. Biogenesis of diatom biosilica is a bottom-up process that occurs in large intracellular compartments termed silica deposition vesicles (SDVs). Investigating the mechanisms of silica morphogenesis has so far been severely limited by the lack of methods for imaging the entire volume of an SDV with high spatial resolution during all stages of development. Here we have developed a method that allows for rapid identification and electron microscopy imaging of many different, full sized SDVs that are in the process of producing biosilica valves. This enabled visualizing the development of characteristic morphological biosilica features with unprecedented spatio-temporal resolution. During early to mid-term development, valve SDVs contained ~ 20 nm sized particles that were primarily associated with the radially expanding rib-like biosilica structures. The results from electron dispersive X-ray analysis suggests that the immature biosilica patterns are silica-organic composites. This supports the hypothesis that silica morphogenesis is dependent on organic biomolecules inside the SDV lumen.

Keywords: *Thalassiosira pseudonana*, *Cyclotella cryptica*, Biosilica, Morphogenesis, Cell wall, Costa, Cribrum pore, Areola pore, Fuloportula, Silica nanoparticle

Introduction

Diatoms are a species-rich lineage of single-celled algae that produce silica-based cell walls with species-specific morphologies. A characteristic feature of diatom biosilica are hierarchical patterns of pores with diameters from the nano- to the micrometer range. The porous patterns equip diatom biosilica with interesting materials properties, including light capturing and the highest specific strength of any known biological material [1–9]. A rapidly increasing number of genome and transcriptome data from diatoms have become available, and several species are readily amenable to genetic manipulation [10]. Therefore diatoms are the prime model systems for

studying the molecular basis of biological silica formation, and genetic engineering methods to further enhance the functionalities of diatom biosilica have been established [7, 11, 12].

Diatom cell walls are constructed from two types of biosilica building blocks termed valves and girdle bands. In the cylindrical cell walls of *Thalassiosira pseudonana* and *Cyclotella cryptica*, which have been studied in the present work, the valves represent the top and bottom lids of the cylinder. The girdle bands are partially overlapping rings of silica that are oriented transversely to the long axis of the cylinder constituting a gap-less connection between the two valves. Regarding the nano- and microarchitecture, the biosilica of valves is much more intricately patterned including hierarchical pore patterns, struts, and tubes, while girdle bands are rather flat, perforated rings. Biogenesis of the valves and girdle bands is tightly linked to the cell cycle with valves only being

*Correspondence: nils.kroeger@tu-dresden.de

¹ B CUBE, Center for Molecular and Cellular Bioengineering, TU Dresden, 01307 Dresden, Germany

Full list of author information is available at the end of the article



© The Author(s) 2020. This article is licensed under a Creative Commons Attribution 4.0 International License, which permits use, sharing, adaptation, distribution and reproduction in any medium or format, as long as you give appropriate credit to the original author(s) and the source, provide a link to the Creative Commons licence, and indicate if changes were made. The images or other third party material in this article are included in the article's Creative Commons licence, unless indicated otherwise in a credit line to the material. If material is not included in the article's Creative Commons licence and your intended use is not permitted by statutory regulation or exceeds the permitted use, you will need to obtain permission directly from the copyright holder. To view a copy of this licence, visit <http://creativecommons.org/licenses/by/4.0/>. The Creative Commons Public Domain Dedication waiver (<http://creativecommons.org/publicdomain/zero/1.0/>) applies to the data made available in this article, unless otherwise stated in a credit line to the data.

produced during cell division, while girdle bands are made exclusively during interphase. Each valve and each girdle band develops inside the cell in a separate compartment termed silica deposition vesicle (SDV). When the formation of an entire valve or girdle band is complete inside its SDV, it is exocytosed to the cell surface and becomes incorporated into the cell wall.

Cell biologists and materials scientist alike have been intrigued by the capability of SDVs to produce intricately patterned biosilica structures [13, 14]. Several models have been put forward regarding the mechanisms for silica morphogenesis in valve SDVs [15–25]. Some models proposed that silica nanoparticles are the building material for biosilica morphogenesis [15], and that proteins and other biomacromolecules in the SDV lumen act as templates in this process [20, 22, 25]. However, to date there is only circumstantial evidence for the existence of silica nanoparticles and organic macromolecules inside SDVs. Using SEM and AFM, the mature cell walls of *Coscinodiscus granii*, *Pinnularia viridis*, and *Hantzschia amphioxys* have been shown to exhibit granular surfaces and seemed to be composed of globular silica particles in the range of 100–200 nm (*C. granii*) and ~40 nm (*P. viridis*, *H. amphioxys*) [26, 27]. In TEM analysis of chemically fixed and sectioned diatoms cells, spherical particles of 12–30 nm diameter were observed at the growing zone of valve SDVs [28]. It was hypothesized that these spherical particles were composed of silica, but no chemical analysis was performed. The presence of organic components inside the SDV lumen was hypothesized based on the biochemical analysis of biosilica preparations that were mainly composed of mature cell walls with only a small proportion of developing silica. The preparations contained long-chain polyamines, polysaccharides, phosphoproteins (silaffins, silacidins), and other proteins (frustulins, pleuralins, cingulins, SiMat proteins) [20, 22, 29–31]. Two of these proteins, silicanin-1 (formerly named SiMat7) and SAP-3 were shown by GFP-tagging to be present in the SDV membrane [32, 33], whereas immunolocalization demonstrated that frustulins and pleuralins are absent from SDVs [34]. For all other organic components it is unclear whether they are present inside the SDV during silica biogenesis or whether they become associated with the mature silica on the cell surface.

A major bottleneck for elucidating the mechanism of biosilica morphogenesis is the lack of detailed structural information about all intermediate stages of biosilica development. Previous attempts took advantage of the possibility to synchronize the diatom cell cycle thereby increasing the fraction of cells with developing SDVs. To allow for the imaging of nanoscale features mainly electron microscopy and in a few cases atomic force

microscopy (AFM) was employed. Access to the developing biosilica structures inside the intracellular SDVs was achieved by two methods. The first method involved cell lysis using strong acids or detergent, which also removed all or most organic material, and allowed for imaging of the immature biosilica by transmission electron microscopy (TEM), scanning electron microscopy (SEM), and AFM [35–38]. As a result, images of the entire volumes of developing biosilica structure, primarily from valves, were obtained. However, the treatment with acid or detergent was prone to introducing artifacts by destroying the SDV membrane and extracting all material from the SDV lumen that is soluble under these conditions. The second method used chemical fixation of cells followed by resin embedment, ultrathin sectioning, and imaging with TEM [28, 34, 39–43]. This allowed for imaging developing biosilica inside the SDV and within the entire cellular context. However, the required chemical treatment is susceptible to introducing artifacts, and imaging substantial fractions or an entire SDV volume has not yet been achieved with this method.

Here, we have investigated the possibility to prepare, rapidly identify, and image by TEM intact valve SDVs from cell lysates of the diatoms *Thalassiosira pseudonana* and *Cyclotella cryptica*. The two diatom species are phylogenetically closely related (Order *Thalassiosirales*), have previously been studied regarding their molecular and cellular mechanisms of silica morphogenesis [12, 20, 37, 38], their genome sequences are available [44, 45] and molecular genetic transformation systems have been established [46, 47]. By comparing the development of the valves in these two model diatom species, we aimed to identify common steps in biosilica morphogenesis of the *Thalassiosirales*.

Results and discussion

Identifying valve SDVs in cell lysates

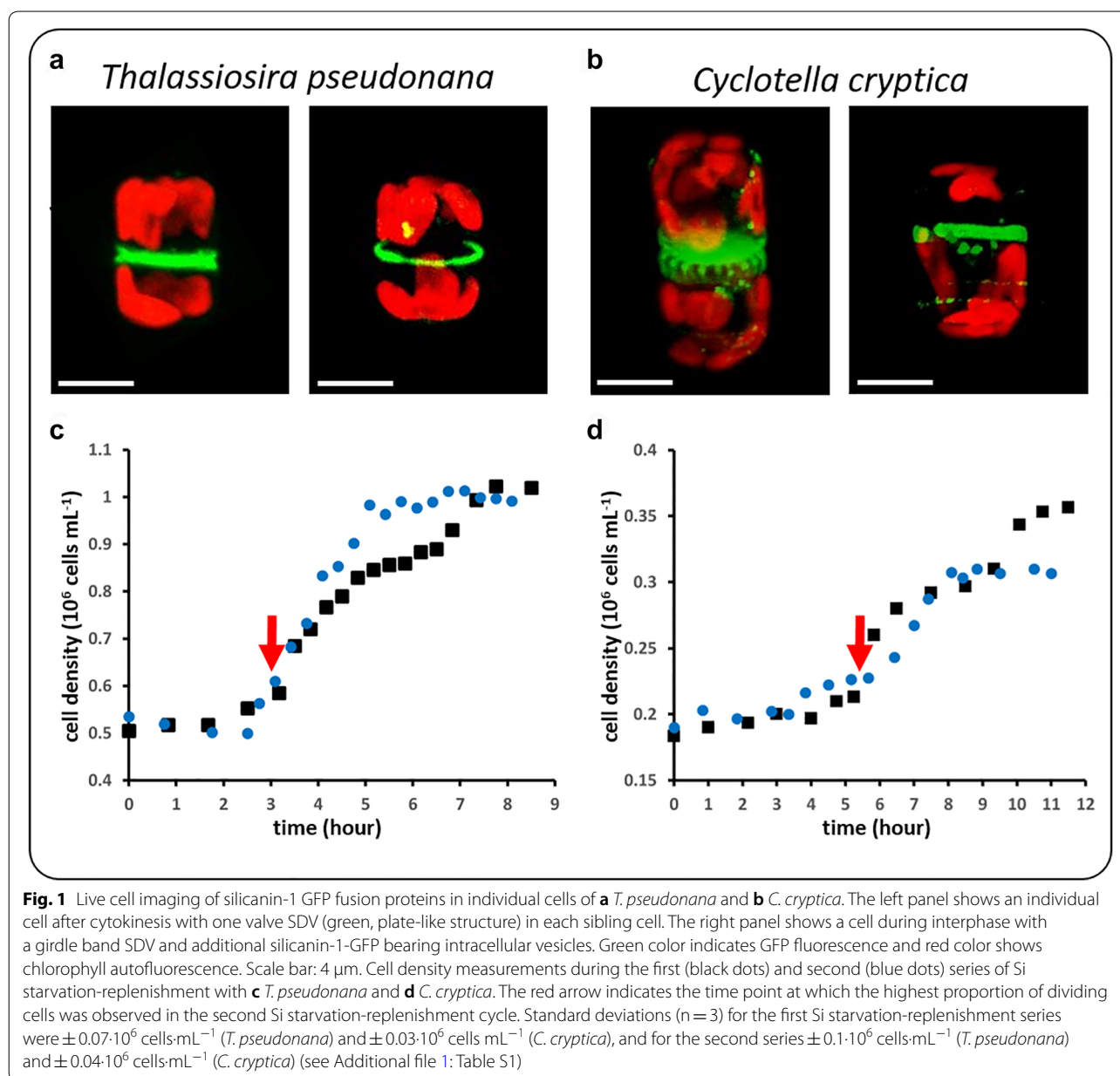
For the rapid identification of valve SDVs in cell lysates, we aimed to establish a fluorescent labeling strategy in combination with correlative fluorescence-electron microscopy imaging, which is outlined in the following. To facilitate following the cell cycle progression *in vivo*, transgenic cell lines were used that expressed C-terminally tagged silicanin-1 (Sin1-GFP^C), which was previously shown to be located in the membrane of *T. pseudonana* valve and girdle band SDVs [32]. By synchronizing the cell culture, the proportion of cells undergoing valve SDV development was enhanced. When the maximum proportion of valve SDV bearing cells was observed, the SDV-specific dye PDMPO was briefly added to the culture to label the silica inside SDVs [48] before it was exocytosed. Cells were gently lysed and the lysate immobilized on a TEM finder grid allowing to rapidly identify

the positions of valve SDVs by fluorescence microscopy searching for PDMPO-labeled structures with plate-like morphology. TEM was then employed for imaging the objects at the identified positions.

A Sin1-GFP^C expressing *T. pseudonana* cell line had previously been generated [32], but a corresponding transgenic *C. cryptica* cell line had to be established here. Previously, gene *g20669.t1* was identified as *Sin1* homologue of *C. cryptica*, because its predicted protein sequence, ccSin1, showed 75.9% global sequence identity to *T. pseudonana* Sin1 [32]. A transgenic *C. cryptica* cell line was produced that expressed C-terminally

GFP-tagged ccSin1 (ccSin1-GFP^C) under control of the *ccSin1* promoter and terminator sequences. Fluorescence microscopy revealed that ccSin1-GFP^C was located in both valve SDVs and girdle band SDVs as well as several other intracellular vesicles (Fig. 1b). These locations match those previously described for Sin1-GFP^C in *T. pseudonana* (Fig. 1a) [32]. Based on the sequence and intracellular location, we concluded that ccSin1 indeed represents the functional homologue of *T. pseudonana* Sin1.

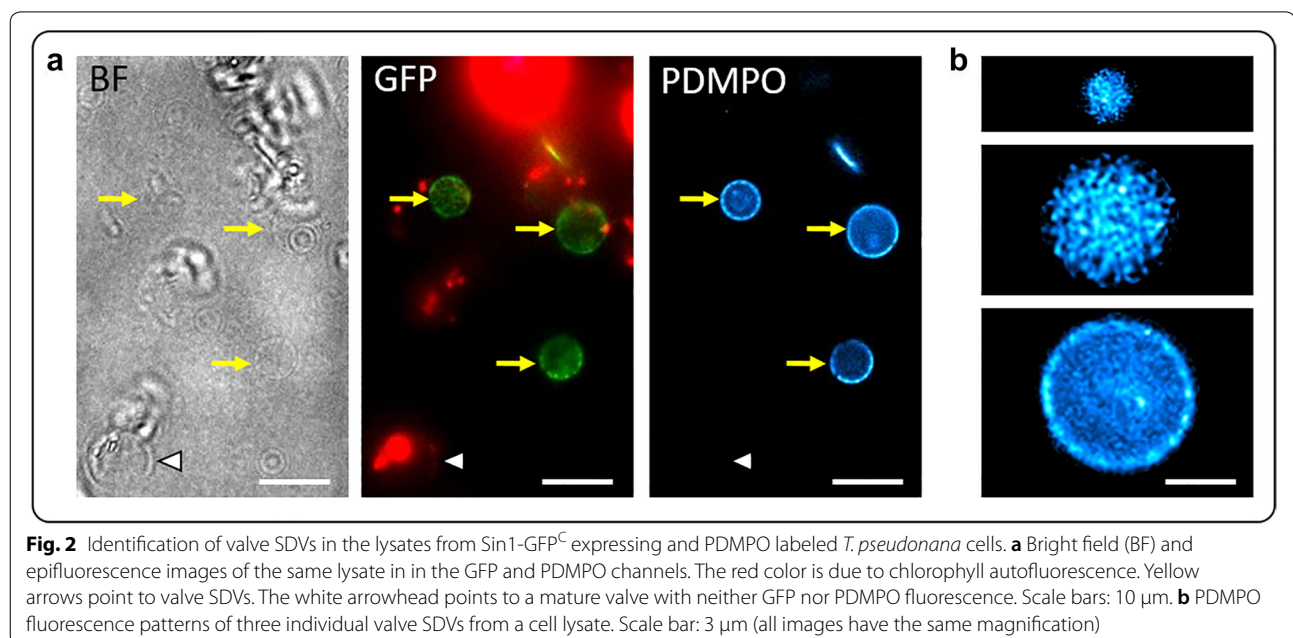
Previously, incubation of diatom cultures in silicic acid-free medium for extended period of times followed



by replenishment of silicic acid (in the following abbreviated Si) has achieved only partial cell cycle synchrony for various diatoms species including *T. pseudonana* and *C. cryptica* [38, 49]. Here, we have investigated the effect of two consecutive Si starvation-replenishment series on the synchrony of cell division in *T. pseudonana* and *C. cryptica*. During the first Si starvation-replenishment series for *T. pseudonana*, an increase in cell density occurred 2.5 h after re-addition of Si (Fig. 1c, black dots). The initial cell density had doubled after 5.5 h, which suggested that each cell underwent one cell division within 3 h. The percentage of dividing cells at several time points after Si replenishment was estimated based on the proportion of cells that exhibited the characteristic valve-shaped Sin1-GFP^C fluorescence in the mid cell region (at each time point 100 cells were examined). The maximum proportion of cells containing valve SDVs was ~30% and was observed 3.5 h after replenishment of Si. After 9 h, the cells were subjected again to Si starvation followed by Si replenishment. This time, the cell number doubled between 2.75 and 5 h after Si replenishment and thus required only 2.25 h (Fig. 1c, blue dots). The maximum proportion of dividing cells was 70% and was reached 3 h after Si replenishment. These data demonstrated that the two consecutive silicon starvation-replenishment series improved the cell division synchrony in *T. pseudonana*. In contrast, for *C. cryptica* one Si starvation-replenishment series achieved better cell cycle synchrony than two consecutive ones. In the first series, cell division started 4.75 h after Si replenishment, and the cell

density had doubled after 10 h (Fig. 1d, black dots). The maximum proportion of dividing cells was observed 5.5 h after Si replenishment and was only 10%. During the second silicon starvation-replenishment cycle, the cell density increased only 50% within 12 h after Si replenishment, and the maximum proportion of dividing cells was only 7% (observed after 6 h; Fig. 1d, blue dots). We assumed, that repeated Si starvation imposes a higher metabolic stress on *C. cryptica* compared to *T. pseudonana*, and thus the growth rate of the former slows down after the second Si starvation period.

To tag valve SDVs with a second fluorescent label, synchronized cells were incubated briefly (10 min) with PDMPO at the time point when the highest proportion of valve SDV bearing cells was present, i.e., 3 and 5.5 h after the second Si replenishment for *T. pseudonana* and *C. cryptica*, respectively (Fig. 1c, d; red arrows). Immediately after PDMPO labelling, the cells were gently lysed, and putative valve SDVs could be readily identified by epifluorescence microscopy as GFP and PDMPO labeled disks (Fig. 2a; yellow arrows). Discs that exhibited much stronger contrast in bright field microscopy than the putative valve SDVs but lacked both GFP and PDMPO fluorescence (Fig. 2b; white arrowhead), were presumed to be mature valves. Inspection of many putative valve SDVs revealed differences in diameters and PDMPO fluorescence patterns (Fig. 2b). Discs with diameters of 2–3 μm showed usually a quite homogeneous distribution of PDMPO fluorescence. In contrast, SDVs with diameters of 4–6 μm showed homogeneous fluorescence only in the central region and exhibited



a more strongly fluorescent rim with a dot-like pattern. We hypothesized that the different types of PDMPO labeled disks represent valve SDVs containing biosilica at different developmental stages. To verify this, a correlative fluorescence approach and transmission electron approach was applied, which revealed that PDMPO and GFP labeled disks indeed contained immature valve biosilica (Fig. 3).

TEM analysis of valve morphogenesis

It is to be expected that silica biogenesis came to a stop when the cells were lysed, because this procedure was performed near 0 °C and involved a >25-fold dilution of the cellular content, which should drastically slow down all metabolic activity. Therefore, it is reasonable to assume that each valve that was immobilized on the TEM grid was in the same developmental stage as at the time point of cell lysis. The valve SDVs were then permanently “frozen” in their developmental stages through washing with H₂O and drying. As a consequence of this preparation method, it was not possible to follow the development of individual valve SDVs. However, since the cells were not in perfect cell cycle synchrony, the lysate contained valves from many (possibly all) different developmental stages. To obtain a detailed view of valve morphogenesis, more than 150 TEM images of valve SDVs of different developmental stages were obtained from *T. pseudonana*. This confirmed that SDVs with a homogenous PDMPO pattern corresponded to earlier developmental stages of the biosilica than those exhibiting intense, dot-patterned PDMPO fluorescence

at the rim (Additional file 2: Fig. S1). An analogous correlative fluorescence microscopy-TEM analysis was performed with lysates from ccSin1-GFP^C expressing and PDMPO labeled *C. cryptica* cells. From these analyses, the sequence of changes in biosilica structure during valve morphogenesis was reconstructed for both *T. pseudonana* and *C. cryptica* (Figs. 4, 5). The general criterion to establish the sequence of valve development was the progression of individual morphological features, such as the dendritic branches, the porous layers, or tube-like structures (called fultoportula). EDX mapping of valve SDVs indicated that all developing morphological features visible in TEM images were silica-based (Additional file 3: Fig. S2). In the following, valve morphogenesis of *T. pseudonana* and *C. cryptica* are comparatively described.

In both species, the smallest discernable biosilica structure is a central silica ring (termed annulus) from which regularly spaced, radial silica ribs (termed costae) emerge (Fig. 4a, 5a). The costae start branching relatively soon after they emerge from the annulus. They have rather rough edges and seem to be composed of an agglomeration of globular particles. As the valve SDV increases in diameter, the costae continue to grow radially in both species (Fig. 4b, c). In *C. cryptica* thinner costae (termed narrow costae) emanate from the much wider primary costae (Fig. 5b). As the SDV diameter increases, the narrow costae grow radially in parallel to the wide costae (Fig. 5c, d).

Already at early stages during costae growth in *T. pseudonana*, the formation of pores with ~20 nm diameter (i.e. cribrum pores) occurs in the valve center (Fig. 4c,

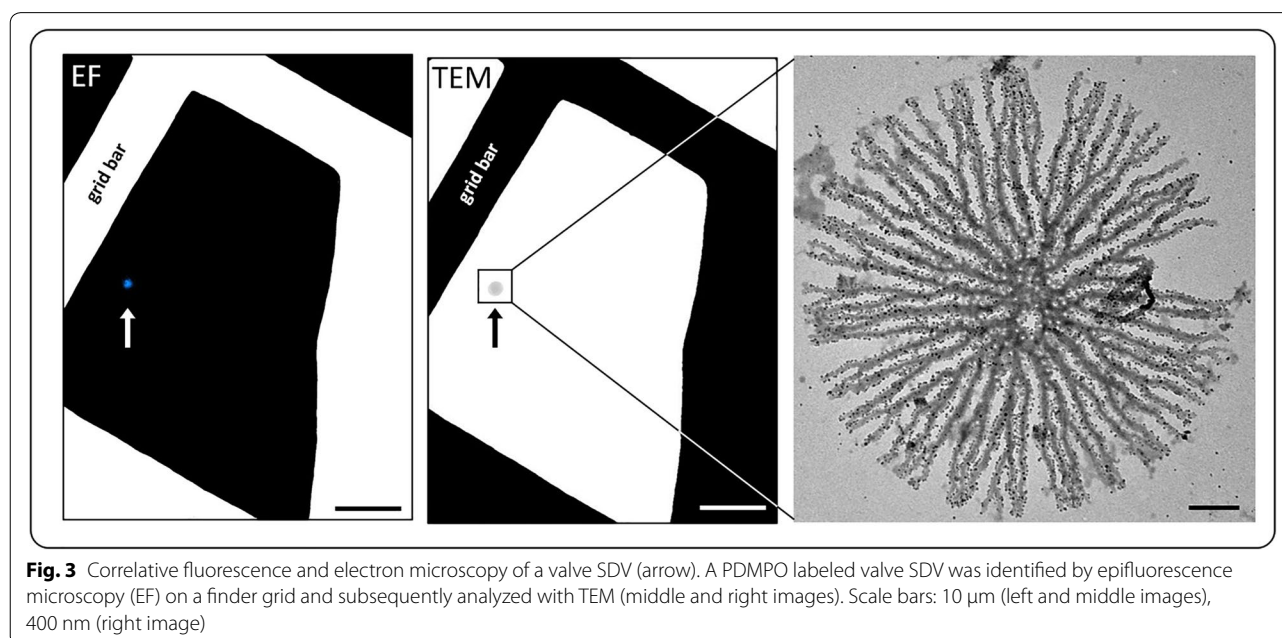


Fig. 3 Correlative fluorescence and electron microscopy of a valve SDV (arrow). A PDMPO labeled valve SDV was identified by epifluorescence microscopy (EF) on a finder grid and subsequently analyzed with TEM (middle and right images). Scale bars: 10 μm (left and middle images), 400 nm (right image)

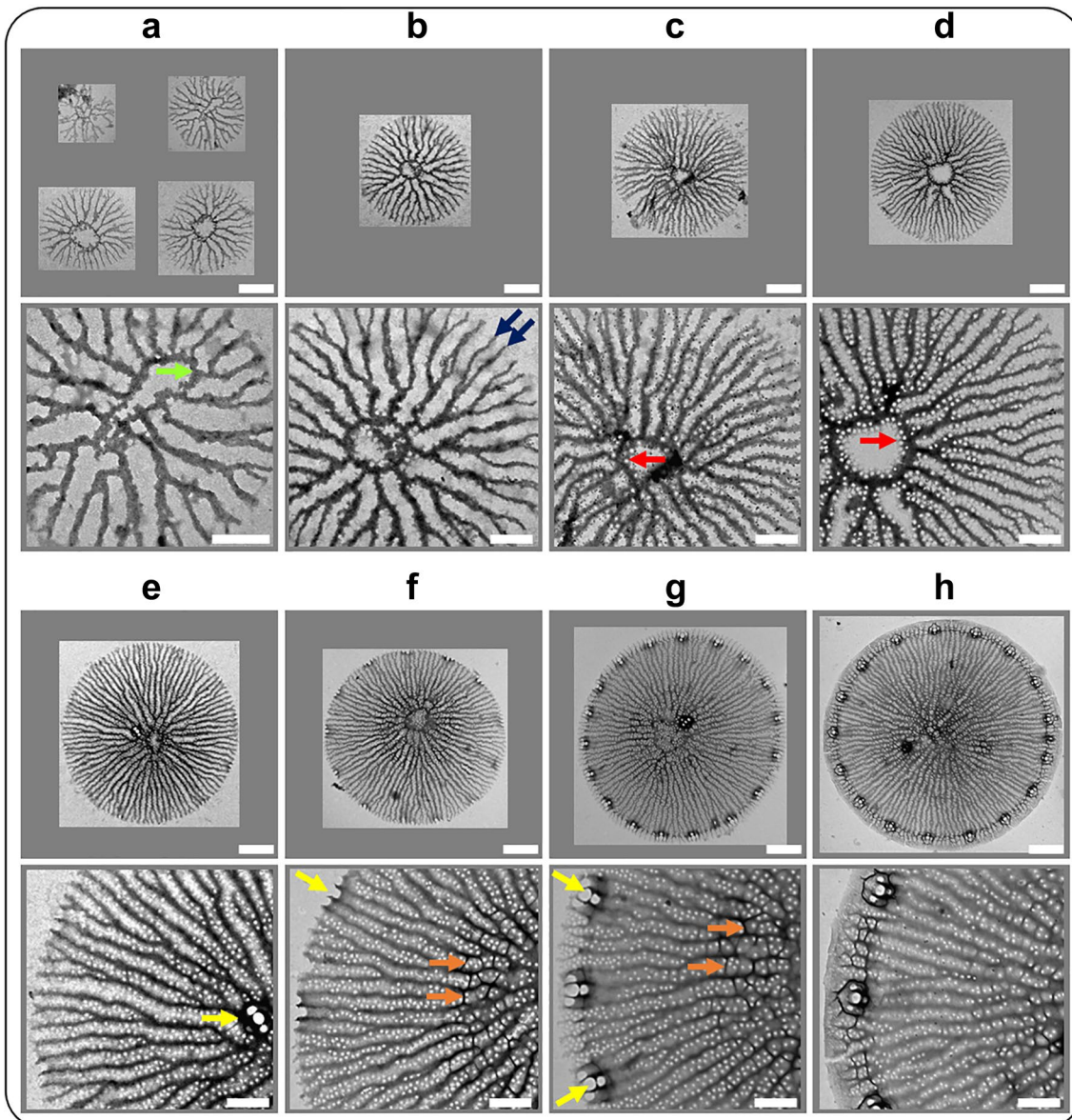


Fig. 4 Valve development in *T. pseudonana*. Different valve SDVs were imaged by TEM and ordered based on the stage of silica structure formation. For each valve, an overview image (top row) and a corresponding detail image (bottom row) is shown. Colored arrows highlight characteristic biosilica features: green = annulus, blue = costa, red = cribrum pore, yellow = fultoportula, orange = areola pore. Scale bars: 1 μm (overview images), 400 nm (detail images)

d). Subsequently, cribrum pore formation propagates radially along the costae and a thin silica layer develops around the pores (Fig. 4d, e) eventually filling the entire space between the costae (Fig. 4f). In *C. cryptica* the formation of cribrum pores that have similar diameters (~ 20 nm) as in *T. pseudonana* also starts in the center relatively early during valve development (Fig. 5c). Cribrum pore formation proceeds radially outward along the wide and narrow costae (Fig. 5c–h). However, as the

space between the costae becomes filled with a layer of silica, 1–3 additional rows of cribrum pores are formed that are not adjacent to any costa (Fig. 5h). In contrast, cribrum pores that are not adjacent to costae are quite rare in *T. pseudonana*.

When the costae have almost reached their full length, the formation of regularly spaced, tube-like structures (each termed fultoportula) is initiated in *T. pseudonana*. Fultoportula formation is highly

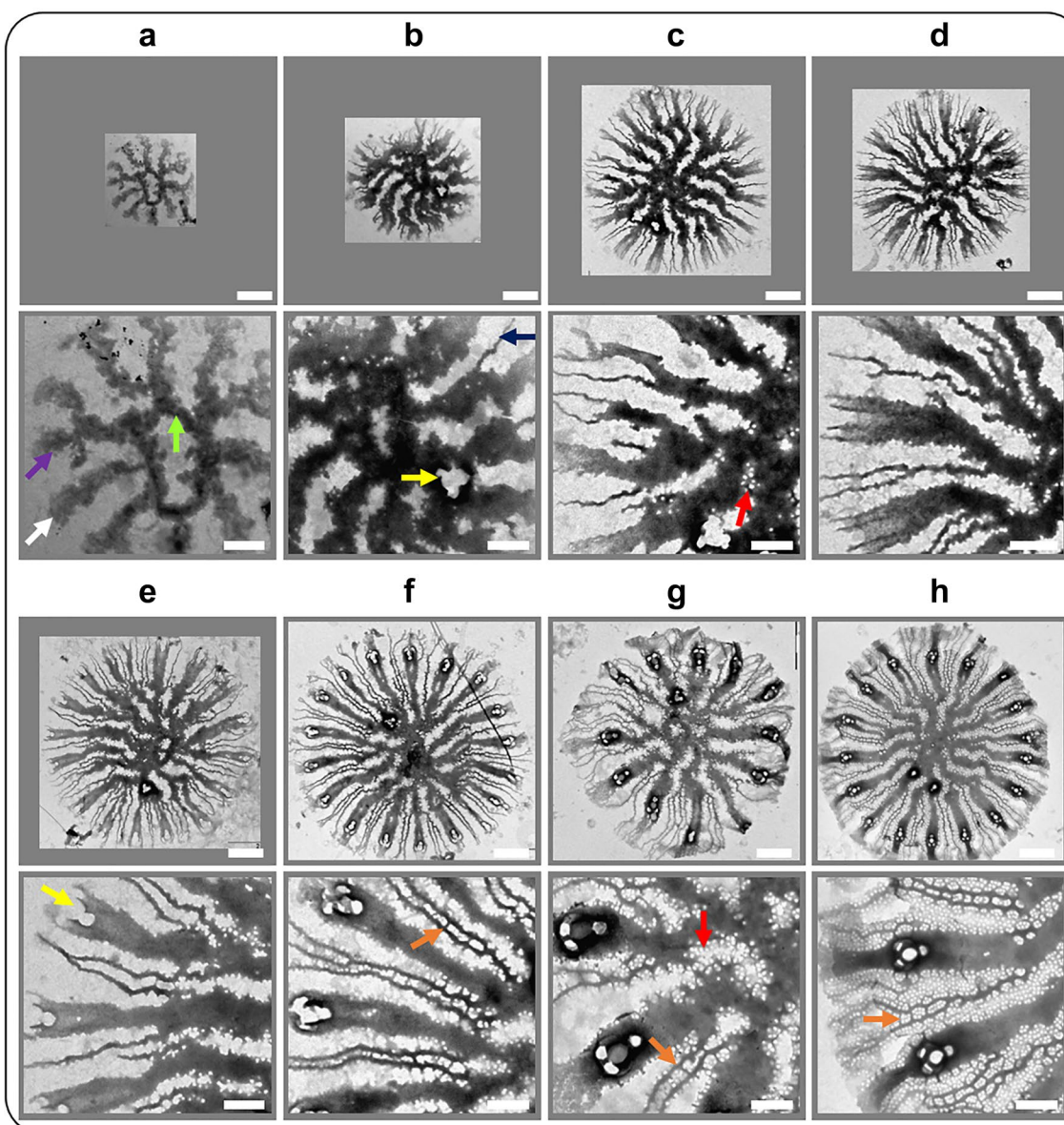


Fig. 5 Valve development in *C. cryptica*. Different valve SDVs were imaged by TEM and ordered based on the stage of silica structure formation. For each valve an overview image (top row) and a corresponding detail image (bottom row) is shown. Colored arrows highlight characteristic biosilica features: green = annulus, purple = wide costa, blue = narrow costae, red = cribrum pore, yellow = fultoportula, orange = areola pore. Scale bars: 1 μm (overview images), 400 nm (detail images)

synchronized throughout the valve and involves the ends of four (rarely three) costae, which cease normal growth and instead develop into a central tube with three satellite pores (Fig. 4f–h). The inter costae space adjacent to the fultoportula is fully silicified lacking cribrum pores (Fig. 4g). In the regions between the developing fultoportulae, costae continue to extend but cease shortly after fultoportulae formation is completed. Termination of the lateral valve growth is

marked by the merging of the costae ends into a patternless, non-porous ring of silica, which represents a continuous margin of the valve (Fig. 4h). In *C. cryptica*, each wide costa develops a fultoportula well before the full length of the costae has been reached (Fig. 5e–h). Both wide and narrow costae continue to grow beyond the position of the fultoportulae before they merge into a patternless continuous ring of silica. Both, in *T. pseudonana* and *C. cryptica* almost 50% of the valves

contain one (rarely two) fulstoportula that is positioned slightly off the valve center (Figs. 4g, h, 5f–h). Formation of these central fulstoportulae always precedes the formation of the fulstoportulae at the periphery of the valve (Figs. 4e, 5b).

When fulstoportulae formation commences in *T. pseudonana*, neighboring costae in the central part of the valve become connected by silica bridges (Fig. 4f, g). As valve development progresses, the number of silica bridges decreases towards the periphery, however, they become particularly prominent close to the valve margin in the spaces between fulstoportulae (Fig. 4h). Two neighboring silica bridges together with the two interjacent costae segments represent so-called areola walls, which together constitute an areola pore. Each areola pore usually encompasses several cribrum pores (Fig. 4f, g).

The formation of fulstoportulae and areolae pores coincides with an apparent increase in thickness of the silica throughout the valve, which has previously been coined “z expansion” [37]. In *C. cryptica*, the silica bridges between neighboring costae start appearing also during fulstoportulae formation (Fig. 5f). In *T. pseudonana* cribrum pore formation in a given area is always completed before silica bridges arise, whereas both these structural

features develop simultaneously in *C. cryptica* (Fig. 5f, g). In some areas it is evident that an areola pore can be completed even before the cribrum pores are formed (Fig. 5f).

Valve morphogenesis in *T. pseudonana* and *C. cryptica* has been investigated before [37, 38]. However, the correlative fluorescence and electron microscopy approach that was established in the present work has enabled the imaging of entire immature valves at an unprecedented number of different developmental stages while they are still encased by the SDV membrane. These include the structures of the annulus and costae at early developmental stages, and the differences between *T. pseudonana* and *C. cryptica* in the timing of the development of cribrum pores and areola pores. Figure 6 schematically summarizes the main steps in the morphogenesis of the valves of *T. pseudonana* and *C. cryptica* to highlight the similarities and differences in structures and development of their valves.

Morphogenesis of cribrum pores in *T. pseudonana*

The cribrum pores of *T. pseudonana* are 22 ± 2 nm (n=200) in diameter and positioned in a seemingly irregular pattern within the silica layer between the costae. In the following we refer to the silica layer between

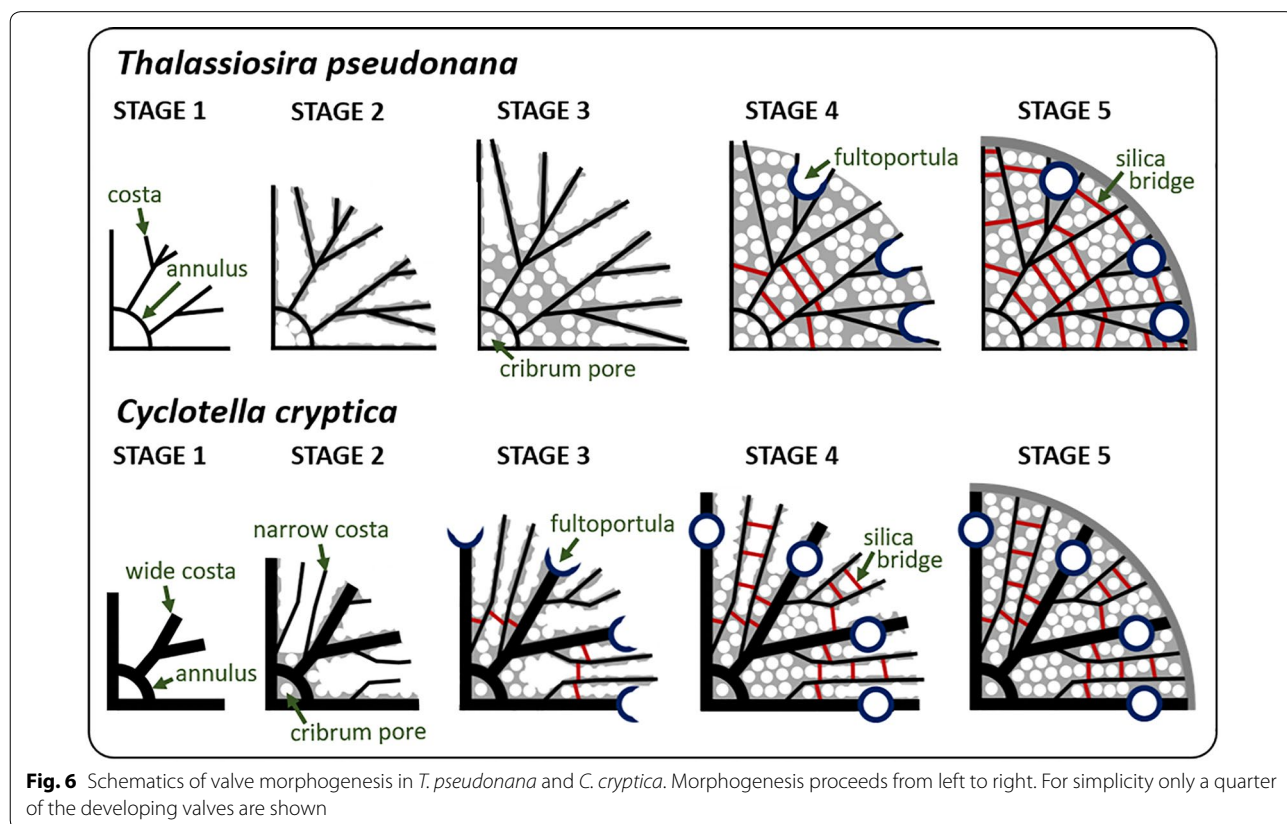


Fig. 6 Schematics of valve morphogenesis in *T. pseudonana* and *C. cryptica*. Morphogenesis proceeds from left to right. For simplicity only a quarter of the developing valves are shown

the costae as cribrum pore layer. From numerous images of immature valves at various stages of development, the morphogenesis of the cribrum pore layer was reconstructed (Fig. 7). Cribrum pore formation always starts along the costae, which are initially rather smooth (Fig. 7a, a'; white arrowheads). The costae develop wave-like edges as silica grows into the space between the costae (Fig. 7b, b'; yellow arrowheads). The wave peaks are fairly regularly spaced and each develops into an anvil shaped structure with the anvil ends elongating parallel to the long-axis of the costa (Fig. 7b, b', c; blue arrowheads). The ends of two neighboring anvils that face each other merge, thus establishing a cribrum pore (Fig. 7c, c'; red arrowheads). The rows of cribrum pores associated with neighboring costae usually have very similar periodicities. The space between the two rows of pores becomes filled with silica, when the distance between the costae is < 120 nm. When neighboring costae are spaced wider than 120 nm, additional cribrum pores can develop

that do not originate from a costa edge (Fig. 7c; green arrowhead).

The elemental composition of biosilica in valve SDVs

In some of the *T. pseudonana* cell lysate preparations, SDVs were observed that contained many spherical nanoparticles with diameters of 19.4 ± 2.4 nm (n = 100) (Fig. 8a–c). The nanoparticles were also observed in some valve SDVs of *C. cryptica* (Additional file 4: Fig. S3). In *T. pseudonana*, the nanoparticles were only observed during cribrum pore formation and were primarily associated with the costae. It has previously been hypothesized that silica nanoparticles are the primary building blocks for biosilica morphogenesis inside the SDV [15, 27, 28]. The hypothesis was based on rather circumstantial evidence that included the presence of electron dense nanoparticles of unknown chemical composition in the growth zones of SDVs [28] (see also Introduction for further information). To investigate the elemental

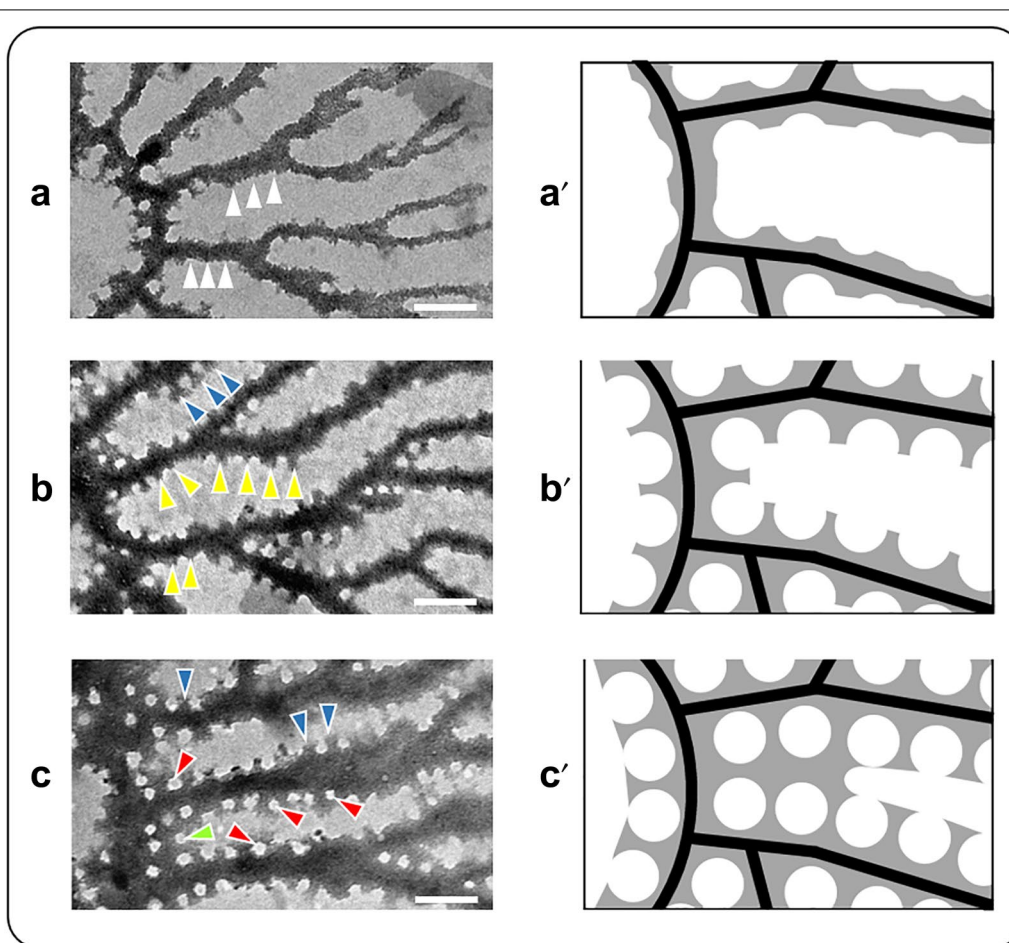


Fig. 7 Morphogenesis of cribrum pores in *T. pseudonana*. Images a–c show TEM micrographs from valve SDVs in different developmental stages, and images a'–c' show schematics of the same developmental stages. The arrowheads point to features that are described in the text. Scale bars: 200 nm

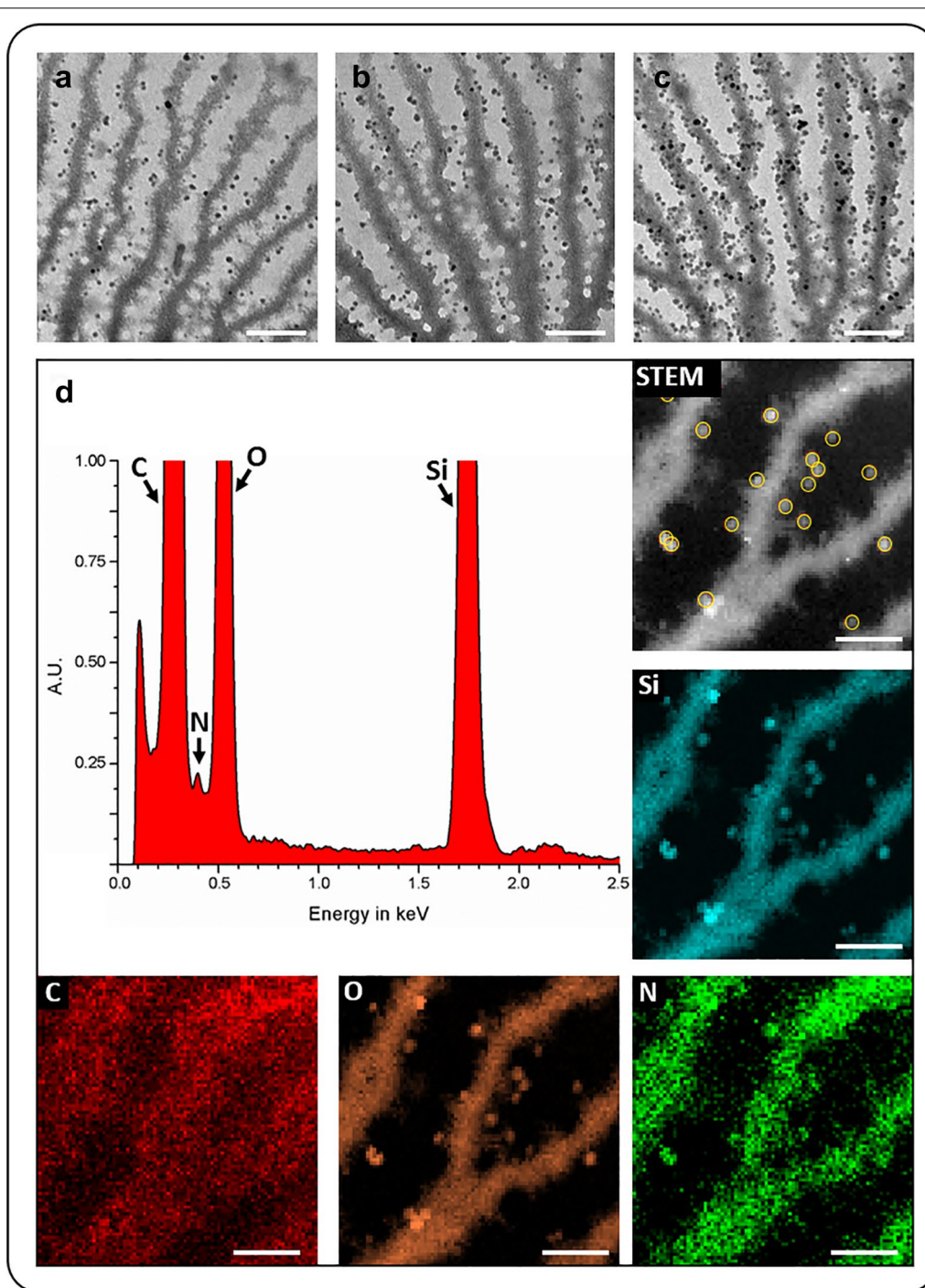


Fig. 8 a–c TEM images of early valve SDVs with associated ~20 nm sized spherical nanoparticles. Scale bars: 200 nm. **d** Scanning transmission electron microscopy (STEM) EDX analysis of several nanoparticles within a single valve SDV. The yellow circles in the STEM image highlight the nanoparticles from which the EDX spectrum was obtained. The elemental maps are depicted with the corresponding chemical symbol. Scale bars: 100 nm

composition of the nanoparticles that were present in our SDV preparations, energy-dispersive X-ray (EDX) spectroscopy was performed. The EDX spectrum of

the nanoparticles (Fig. 8d) showed characteristic signals for carbon (0.27 keV), nitrogen (0.40 keV), oxygen (0.52 keV), and silicon (1.75 keV). The silicon and oxygen

signals are indicative of the nanoparticles being silica based. The nitrogen signal inside the nanoparticles might hint towards the presence of proteins, long-chain polyamines, and/or amino sugar bearing polysaccharides, all of which are known to be associated with mature diatom biosilica [20–22]. However, we cannot rule out that the nitrogen signal originated from nitrogen containing metabolites (e.g., amino acids) or a purely inorganic compound (e.g., nitrate, ammonia). EDX mapping of the valve SDVs confirmed that the costae and the nanoparticles are silica- and nitrogen based (Fig. 8d). The carbon signal in the spectrum originated mainly from the formvar coated grid surface (note that formvar is free of nitrogen and silicon), yet the EDX map clearly indicated the presence of carbon also in the costae (Fig. 8d). This result supports the presence of organic components inside the valve SDV. The silica nanoparticles could not be clearly identified in the carbon map, presumably due to the high carbon signal of the background.

To investigate the elemental composition of the immature valve biosilica independent of the surrounding SDV lipid bilayer and other SDV components that are not or only loosely attached with the developing silica structures, the lysate was extracted with sodium dodecyl sulfate (SDS) before immobilization on a formvar coated grid. Immature valve biosilica could still be easily identified on the grid, because the PDMPO molecules are tightly incorporated into the silica matrix [48]. As expected, the EDX spectrum (Fig. 9) of the detergent-treated, immature valve biosilica showed signals for carbon (0.27 keV), oxygen (0.52 keV), nitrogen, (0.4 keV) and silicon (1.75 keV). Additional signals for cobalt (0.77 keV), aluminum (1.48 keV), and phosphorus (2.0 keV) were obtained. The cobalt signal in the EDX spectrum originated from excitations in the pole piece of the microscope rather than the sample. The presence of aluminum in the immature valve biosilica was not unexpected as this element was previously found in biosilica isolated from both naturally grown and cultivated diatoms [50, 51]. Carbon, nitrogen and phosphorous are clearly co-located with the silica in the immature valve, which is consistent with the previously proposed presence of long-chain polyamines and highly phosphorylated proteins (i.e., silaffins and silacidins) [20, 22]. The phosphorous signal might also be caused by the presence of inorganic phosphate, which has previously been found associated with mature biosilica in the diatom *Coscinodiscus granii* [52].

Conclusion

In the present study we developed an easy method for labeling and imaging SDVs that should in principle be applicable to all diatoms. A limitation of the method is the sensitivity for PDMPO detection, which makes it difficult to identify very early stages of valve SDVs. The first-time demonstration by EDX analysis of the presence of silica nanoparticles inside *T. pseudonana* and *C. cryptica* SDVs was not entirely unexpected, but was not observed in all preparations. We hypothesize, that the silica nanoparticles may be remnants of highly hydrated liquid nanodroplets that are composed of an intimate mixture of polysilicic acids and organic macromolecules. In SDVs *in vivo*, the Si-organic nanodroplets may provide the material for growth of the costae and the biogenesis of the cribrum plates. The latter develop from the edges of the costae, where the nanoparticles were primarily observed (see Fig. 7). It is conceivable that during relatively uncontrolled drying of our samples, such nanodroplets might often disintegrate or form layers on the costae surfaces rather than yielding spherical nanoparticles. This would explain the inconsistent presence of the silica nanoparticles in our SDV preparations. To finally resolve this question, it will be essential to avoid drying artifacts by performing cryo-EM analysis of valve SDVs.

The EDX analyses provided the first direct demonstration that the biosilica inside SDVs is intimately associated with non-silica components. The C, N and P content of developing biosilica is consistent with the presence of long-chain polyamines and phosphoproteins, which so far have only been located in the mature biosilica of cell walls. Although we regard it unlikely, the possibility cannot be excluded that the P and N content in immature valve biosilica is derived from purely inorganic components. In future research, it will therefore be necessary to demonstrate the presence of biomacromolecules in valve SDVs through more direct methods like immunolocalization or mass spectrometry.

Methods

Chemicals and enzymes

Oligonucleotides were purchased from Eurofins Genomics. The enzymes for molecular genetics and phenylmethylsulfonyl fluoride (PMSF) were purchased from Thermo Fisher Scientific. Hydroxyethyl-piperazineethane-sulfonic acid (Hepes), sodium chloride, and sucrose were obtained from Sigma-Aldrich. Ampicillin was obtained from Merck and nourseothricin from Jena Bioscience. The TEM gold finder grids were purchased from Science Service. PDMPO was obtained from AAT Bioquest and the sodium dodecyl sulfate (SDS) was

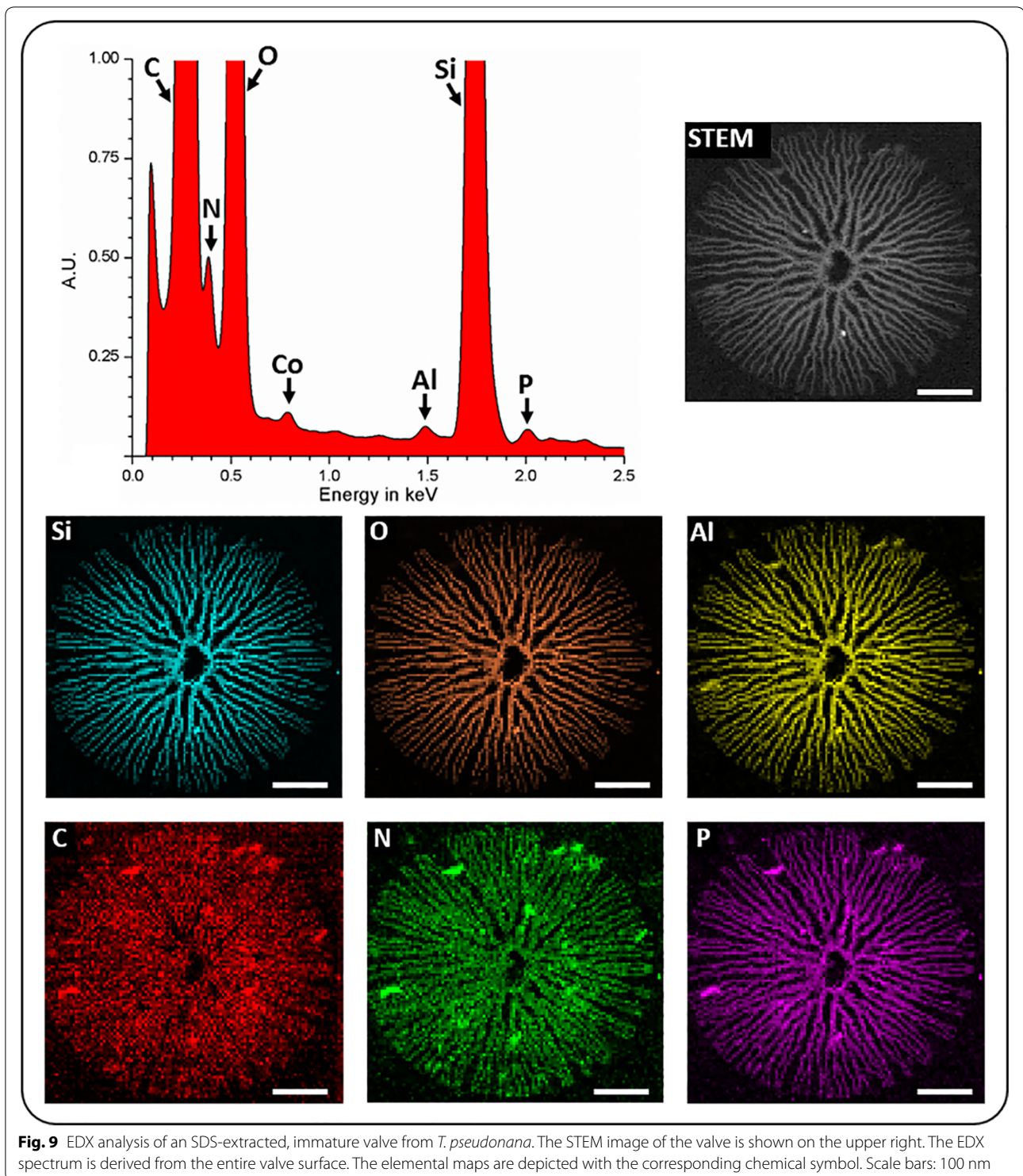


Fig. 9 EDX analysis of an SDS-extracted, immature valve from *T. pseudonana*. The STEM image of the valve is shown on the upper right. The EDX spectrum is derived from the entire valve surface. The elemental maps are depicted with the corresponding chemical symbol. Scale bars: 100 nm

obtained from Carl Roth. MiliQ-purified H₂O was used for all experiments.

Cell culturing

The wild type and transformant strains of *T. pseudonana* CCMP1335 and *C. cryptica* CCMP332 were maintained in artificial seawater (ASW) according to Darley and

Volcani [53] with modifications as described in Additional file 5: Supporting Information. Cells were cultured at 18 °C and 5000 lx in a 12 h/12 h day-night cycle.

Generating transgenic *C. cryptica* expressing ccSin1-GFP

For C-terminal GFP-tagging of the *ccSin1* gene (ID: g20669) the *ccSin1* promoter region (978 bp upstream of the start ATG) and the *ccSin1* coding region was amplified from genomic DNA using the sense primer 5'-ACTTGGGCCCCCTTCATGGCACCGGTGAGG-3' (*ApaI* site underlined) and the antisense primer 5'-GATCCCCGGGGCCATGGCACCACCCTGTC-3' (*SmaI* site underlined). The resulting PCR product was digested with *ApaI* and *SmaI* and introduced into the *ApaI* and *EcoRV* sites of pTpNR-GFPHpaI/fcpNat(-NotI) [29] generating pPccSin1-GFP-/fcpNAT(-NotI). The *ccSin1* terminator region (488 bp downstream of the stop codon) was amplified from genomic DNA using the sense primer 5'-ATCGCGGCCGCAGGTCATCGCTTGAGCTGGCAC-3' (*NotI* site underlined) and the antisense primer 5'-TCAGTTAACTTGACTGTCTCTCAAAGTCCAGCG-3' (*HpaI* site underlined) and introduced into the *NotI* and *HpaI* sites of pPccSin1-GFP-/fcpNAT(-NotI) generating the final expression plasmid pPccSin1-ccSin1-GFPC-TccSin1/fcpNAT(-NotI). The sequences were confirmed by DNA sequencing (Eurofins). In the plasmid expression of the *ccSin1-GFP fusion gene* is under control of the endogenous *ccSin1* regulatory sequences. The biolistic transformation of *C. cryptica* and the selection of nourseothricin resistant transformants was performed as described previously [54].

Cell synchronization, PDMPO labeling, and cell lysis

All cell density measurements were done in triplicate using the TC10™ Automated Cell Counter (Bio-Rad). Diatom cells were grown in 300 mL ASW to a cell density of 2.0–5.0 × 10⁵ cells mL⁻¹. The cells were pelleted by centrifugation (3000 xg, 10 min), resuspended in 240 mL Si-free ASW, pelleted again, resuspended in 300 mL Si-free ASW, and incubated for 16 h (12 h dark, 4 h light). During silicon starvation, the cell culture was in a polycarbonate flask under constant aeration. Subsequently, Na₂SiO₃ was added to the culture at a final concentration of 200 μM, and the aeration was turned off. *T. pseudonana* and *C. cryptica* cells were incubated in constant light for 9 and 10 h, respectively, by which time the cell density had doubled. The cells were then subjected to a second silicon starvation period by pelleting 150 mL of the cell culture, washing the cells with Si-free ASW as above, and the resuspension in 300 mL Si-free ASW. The cell culture was incubated for 16 h (12 h dark, 4 h light) under constant aeration in a polycarbonate flask. Subsequently, Na₂SiO₃ was added to the cell culture at a final

concentration of 200 μM and the aeration was stopped. Three hours (*T. pseudonana*) or 5.5 h (*C. cryptica*) after Na₂SiO₃ addition, the entire cell culture was centrifuged at 3000 xg for 10 min, resuspended in 30 mL ASW, and PDMPO was added to a final concentration of 1 μM. After 10 min incubation under constant light, the cells were centrifuged (3000 xg, 10 min) and the pellet was resuspended in 6 ml of lysis buffer (50 mM Hepes-NaOH pH 7.5, 150 mM NaCl, 50 mM Sucrose, 100 μM PMSF). The cell suspension was distributed in 750 μl aliquots into eight 2 ml eppendorf tubes, and 300 μL of nitric acid-cleaned glass beads (Ø 0.2 mm, Retsch) were added. The cells were vigorously vortexed 3 times for 30 s each, the supernatants were transferred into a fresh tube and kept on ice until further use.

Confocal fluorescence microscopy

For imaging, 10 μl of a cell suspension or cell lysate were spotted onto a 22 mm × 50 mm coverslip and overlaid with a thin agarose slice (1% in ASW medium). A Zeiss LSM780 inverted confocal microscope with a Zeiss Plan-Apochromat 63 × (1.4) oil DIC M27 objective was used for image acquisition. GFP and chloroplast autofluorescence were excited with a 488 nm laser line (power set to 1.0%), a MBS 488 beam splitter, and a 32-channel GaAsP spectral detector. Two channels were used to image GFP (491–535 nm) separated from chloroplast autofluorescence (655–721 nm).

Alignment of fluorescence and electron microscopy

A 10 μl drop of the cell lysate was spotted on a Formvar-coated gold finder grid for 1 h. The grid was washed 3 times with lysis buffer (50 mM Hepes pH 7.5, 150 mM NaCl, 50 mM Sucrose, 100 μM PMSF) and placed on a glass slide with the sample facing up. The locations of valve SDVs on the grid were identified by PDMPO fluorescence using a 63x oil objective on a Zeiss Axiovert 200 inverted microscope equipped with a PDMPO filter (excitation 365–395 nm, emission 530–535 nm). Images of the fluorescent valve SDVs with nearby grid bars or letters were taken to document the location for electron microscopy. The grid was then washed 3 times with water and dried by removing the majority of the water with a piece of filter paper followed by air drying overnight. For electron microscopy, the grids were analyzed using a Morgagni 268D (FEI) instrument at an acceleration voltage of 80 kV. SDV positions were identified using the position information from the fluorescence microscopy.

STEM-EDX measurements on valve SDVs

Valve SDVs were localized on a formvar-coated gold grid as described above. Early valve SDVs with associated nanoparticles were analyzed using EDX spectroscopy.

The local elemental concentrations have been analyzed using a JEOL JEM-F200 operated at 200 kV equipped with a dual 100 mm² window-less silicon drift detector. Scanning transmission electron microscope images have been acquired with a convergence semi-angle of 12 mrad. The EDX spectra have been denoised with principal component analyses (PCA) using 20 components [55].

Detergent treatment of valve SDVs for TEM-EDX analysis

Prior to immobilization on the TEM grid, the cell lysate was incubated with 2% (w/v) SDS for 20 min at room temperature. The SDS-treated lysate was immobilized on a Formvar-coated gold grid and analyzed by STEM-EDX as described above.

Supplementary information

Supplementary information accompanies this paper at <https://doi.org/10.1186/s42833-020-00017-8>.

Additional file 1: Table S1. Raw data of the cell density measurements over time in the cell cycle synchronization experiments.

Additional file 2: Figure S1. Comparison of PDMPO fluorescence pattern and biosilica structure by TEM in *T. pseudonana* valve SDVs.

Additional file 3: Figure S2. STEM imaging and EDX analysis of *T. pseudonana* valve SDVs from different developmental stages.

Additional file 4: Figure S3. TEM images of valve SDVs from *C. cryptica* containing ~20 nm sized spherical nanoparticles.

Additional file 5. Supporting information.

Abbreviations

AFM: Atomic force microscopy; ASW: Artificial seawater; DLA: Diffusion limited aggregation; EDX: Energy dispersive x-ray spectroscopy; EF: Epifluorescence microscopy; GFP: Green fluorescent protein; Hepes: Hydroxyethyl-piperazineethane-sulfonic acid; keV: Kilo electron volt; LCPA: Long chain polyamines; PCA: Principal component analyses; PCR: Polymerase chain reaction; PDMPO: 2-(4-Pyridyl)-5-((4-(2-dimethylaminoethylaminocarbonyl)methoxy)phenyl)oxazole; PMSF: Phenylmethylsulfonyl fluoride; SDS: Sodium dodecyl sulfate; SDV: Silica deposition vesicle; SEM: Scanning electron microscopy; Sin1: Silicinin-1; STEM: Scanning transmission electron microscopy; TEM: Transmission electron microscopy.

Acknowledgements

We are indebted to Paul Bomans and Nico Sommerdijk (Eindhoven Institute of Technology, The Netherlands) for initial help with elemental analysis of valve SDVs, Jennifer Klemm (TU Dresden) for help with *C. cryptica* transformation, Damian Pawolski (TU Dresden) for help with TEM analysis, Alexander Kotzsch (TU Dresden) for confocal microscopy analysis, and Nicole Poulsen (TU Dresden) for designing the ccSin1-GFP expression vector and critically reading the manuscript. Expert support was provided by the Light Microscopy Facility and the Electron Microscopy Facility of the Center for Cellular and Molecular Bioengineering (TU Dresden).

Author's contributions

NK and CH conceived the project, designed experiments, analysed data, and wrote the paper. CH and JH performed experiments. PF designed experiments and analysed data. DP performed experiments and analysed data. BR supervised the STEM/EDX data analysis. All authors have read and approved the manuscript.

Funding

This work was funded by the Deutsche Forschungsgemeinschaft (DFG) through Research Unit 2038 "NANOMEET" (DFG Grant KR 1853/6-2), which provided the resources for the design of the study as well as collection, analysis, and interpretation of the data. Open access funding provided by Projekt DEAL.

Availability of data and materials

The authors declare that all data supporting the findings of this study are available within the article and its supplementary information or are available from the corresponding author upon request. The source data for Fig. 1C, D are available as Additional file 1: Table S1.

Competing interests

The authors declare that they have no competing interests.

Author details

¹ B CUBE, Center for Molecular and Cellular Bioengineering, TU Dresden, 01307 Dresden, Germany. ² Cluster of Excellence Physics of Life, TU Dresden, 01062 Dresden, Germany. ³ Faculty of Chemistry and Food Chemistry, Technische Universität Dresden, 01062 Dresden, Germany. ⁴ Leibniz-Institut für Polymerforschung Dresden e.V., 01069 Dresden, Germany. ⁵ Dresden Center for Nanoanalysis (DCN), Center for Advancing Electronics Dresden (cfaed), TU Dresden, 01069 Dresden, Germany.

Received: 15 April 2020 Accepted: 4 August 2020

Published online: 28 August 2020

References

- Raven JA. The Transport and Function of Silicon in Plants. *Biol Rev.* 1983;58(2):179–207.
- Assmy P, Smetacek V, Montresor M, Klaas C, Henjes J, Strass VH, et al. Thick-shelled, grazer-protected diatoms decouple ocean carbon and silicon cycles in the iron-limited Antarctic Circumpolar Current. *Proc Natl Acad Sci USA.* 2013;110(51):20633–8.
- De Tommasi E, Gielis J, Rogato A. Diatom frustule morphogenesis and function: a multidisciplinary survey. *Mar Genomics.* 2017;35(October):1–18.
- Parkinson J, Gordon R. Beyond micromachining: the potential of diatoms. *Trends Biotechnol.* 1999;17(5):190–6.
- Nassif N, Livaige J. From diatoms to silica-based biohybrids. *Chem Soc Rev.* 2011;40(2):849–59.
- Gordon R, Losic D, Tiffany MA, Nagy SS, Sterrenburg FAS. The Glass Menagerie: diatoms for novel applications in nanotechnology. *Trends Biotechnol.* 2009;27(2):116–27.
- Kröger N, Brunner E. Complex-shaped microbial biominerals for nanotechnology. *Wiley Interdiscip Rev Nanomed Nanobiotechnol.* 2014;6(6):615–27.
- Losic D, Mitchell JG, Voelcker NH. Diatomaceous lessons in nanotechnology and advanced materials. *Adv Mater.* 2009;21(29):2947–58.
- Jeffryes C, Campbell J, Li H, Jiao J, Rorrer G. The potential of diatom nanotechnology for applications in solar cells, batteries, and electroluminescent devices. *Energy Environ Sci.* 2011;4(10):3930–41.
- Huang W, Daboussi F. Genetic and metabolic engineering in diatoms. *Philos Trans R Soc B Biol Sci.* 2017;372:1728.
- Delalat B, Sheppard VC, Rasi Ghaemi S, Rao S, Prestidge CA, McPhee G, et al. Targeted drug delivery using genetically engineered diatom biosilica. *Nat Commun.* 2015;6:8791.
- Hildebrand M, Lerch SJL, Shrestha RP. Understanding diatom cell wall silicification-moving forward. *Front Mar Sci.* 2018;5:1–19.
- Pickett-Heaps JD, Schmid AMM, Edgar LA. The cell biology of diatom valve formation. *Progr Phycol Res.* 1990;7:1–168.
- Losic D. Diatom nanotechnology: progress and emerging applications. 1st ed. London: Royal Society of Chemistry; 2017.
- Gordon RM, Drum RW. The chemical basis of diatom morphogenesis. *Int Rev Cytol.* 1994;150:243–372.
- Parkinson J, Brechet Y, Gordon R. Centric diatom morphogenesis: a model based on a DLA algorithm investigating the potential role of microtubules. *Biochim Biophys Acta Mol Cell Res.* 1999;1452(1):89–102.

17. Cox E, Willis L, Bentley K. Integrated simulation with experimentation is a powerful tool for understanding diatom valve morphogenesis. *Biosystems*. 2012;109(3):450–9.
18. Tesson B, Hildebrand M. Extensive and intimate association of the cytoskeleton with forming silica in diatoms: control over patterning on the meso- and micro-scale. *PLoS ONE*. 2010;5(12):e14300.
19. Schmid AMM. Aspects of morphogenesis and function of diatom cell walls with implications for taxonomy. *Protoplasma*. 1994;181(1–4):43–60.
20. Sumper M, Brunner E. Silica biomineralisation in diatoms: the model organism *Thalassiosira pseudonana*. *ChemBioChem*. 2008;9(8):1187–94.
21. Chiovitti A, Harper RE, Willis A, Bacic A, Mulvaney P, Wetherbee R. Variations in the substituted 3-linked mannans closely associated with the silicified walls of diatoms. *J Phycol*. 2005;41(6):1154–61.
22. Kröger N, Poulsen N. Diatoms—from cell wall biogenesis to nanotechnology. *Annu Rev Genet*. 2008;42:83–107.
23. Poulsen N, Sumper M, Kröger N. Biosilica formation in diatoms: characterization of native silaffin-2 and its role in silica morphogenesis. *Proc Natl Acad Sci*. 2003;100(21):12075–80.
24. Poulsen N, Kröger N. Silica morphogenesis by alternative processing of silaffins in the diatom *Thalassiosira pseudonana*. *J Biol Chem*. 2004;279(41):42993–9.
25. Pawolski D, Heintze C, Mey I, Steinem C, Kröger N. Reconstituting the formation of hierarchically porous silica patterns using diatom biomolecules. *J Struct Biol*. 2018;204(1):64–74.
26. Crawford SA, Higgins MJ, Mulvaney P, Wetherbee R. Nanostructure of the diatom frustule as revealed by atomic force and scanning electron microscopy. *J Phycol*. 2001;37(4):543–54.
27. Noll F, Sumper M, Hampp N. Nanostructure of Diatom Silica Surfaces and of Biomimetic Analogues. *Nano Lett*. 2002;2(2):91–5.
28. Schmid AMM, Schulz D. Wall morphogenesis in diatoms: deposition of silica by cytoplasmic vesicles. *Protoplasma*. 1979;100(3–4):267–88.
29. Kotzsch A, Pawolski D, Milentyev A, Shevchenko A, Scheffel A, Poulsen N, et al. Biochemical composition and assembly of biosilica-associated insoluble organic matrices from the diatom *Thalassiosira pseudonana*. *J Biol Chem*. 2016;291(10):4982–97.
30. Scheffel A, Poulsen N, Shian S, Kröger N. Nanopatterned protein microrings from a diatom that direct silica morphogenesis. *Proc Natl Acad Sci USA*. 2011;108(8):3175–80.
31. Brunner E, Richthammer P, Ehrlich H, Paasch S, Simon P, Ueberlein S, et al. Chitin-based organic networks: an integral part of cell wall biosilica in the diatom *Thalassiosira pseudonana*. *Angew Chemie Int Ed*. 2009;48(51):9724–7.
32. Kotzsch A, Gröger P, Pawolski D, Bomans PHH, Sommerdijk NAJM, Schlierf M, et al. Silicanin-1 is a conserved diatom membrane protein involved in silica biomineralization. *BMC Biol*. 2017;15(1):9–11.
33. Tesson B, Lerch SJL, Hildebrand M. Characterization of a new protein family associated with the silica deposition vesicle membrane enables genetic manipulation of diatom silica. *Sci Rep*. 2017;7(1):1–13.
34. Kröger N, Wetherbee R. Pleuralins are involved in theca differentiation in the diatom *Cylindrotheca fusiformis*. *Protist*. 2000;151(3):263–73.
35. Idei M, Sato S, Tamotsu N, Mann DG. Valve morphogenesis in *Diploneis smithii* (Bacillariophyta). *J Phycol*. 2018;54(2):171–86.
36. Cox EJ. Variation in patterns of valve morphogenesis between representatives of six biraphid diatom genera (Bacillariophyceae). *J Phycol*. 1999;35(6):1297–312.
37. Hildebrand M, York E, Kelz JI, Davis AK, Frigeri LG, Allison DP. Nanoscale control of silica morphology and three-dimensional structure during diatom cell wall formation. *J Mater Res*. 2006;21(10):2689–98.
38. Tesson B, Hildebrand M. Dynamics of silica cell wall morphogenesis in the diatom *Cyclotella cryptica*: substructure formation and the role of microfilaments. *J Struct Biol*. 2010;169(1):62–74.
39. Drum RW, Pankratz HS. Post mitotic fine structure of *Gomphonema parvulum*. *J Ultrastruct Res*. 1964;10:217–23.
40. Pickett-Heaps JD. Cell division and morphogenesis of the centric diatom *Chaetoceros decipiens* (Bacillariophyceae) II. Electron microscopy and a new paradigm for tip growth. *J Phycol*. 1998;34(6):995–1004.
41. Pickett-Heaps JD, Kowalski SE. Valve morphogenesis and the microtubule center of the diatom *Hantzschia amphioxys*. *Eur J Cell Biol*. 1981;25(1):150–70.
42. Chiappino ML, Volcani BE. Studies on the biochemistry and fine structure of silicium shell formation in diatoms. *Protoplasma*. 1977;93:205–21.
43. Pickett-Heaps JD, Tippit D, Andreezzi J. Cell division in the pennate diatom *Pinnularia*. IV. Valve morphogenesis. *Biol Cell*. 1979;35(2):199–206.
44. Armbrust EV, Berges JA, Bowler C, Green BR, Martinez D, Putnam NH, et al. The genome of the diatom *Thalassiosira pseudonana*: ecology, evolution, and metabolism. *Science*. 2004;306(5693):79–86.
45. Traller JC, Cokus SJ, Lopez DA, Gaidarenko O, Smith SR, McCrow JP, et al. Genome and methylome of the oleaginous diatom *Cyclotella cryptica* reveal genetic flexibility toward a high lipid phenotype. *Biotechnol Biofuels*. 2016;9(1):1–20.
46. Poulsen N, Chesley PM, Kröger N. Molecular genetic manipulation of the diatom *Thalassiosira pseudonana* (Bacillariophyceae). *J Phycol*. 2006;42(5):1059–65.
47. Dunahay TG, Jarvis EE, Roessler PG. Genetic Transformation of the diatoms *Cyclotella cryptica* and *Navicula saprophila*. *J Phycol*. 1995;31(6):1004–12.
48. Shimizu K, Del Amo Y, Brzezinski MA, Stucky GD, Morse DE. A novel fluorescent silica tracer for biological silicification studies. *Chem Biol*. 2001;8(11):1051–60.
49. Hildebrand M, Frigeri LG, Davis AK. Synchronized Growth of *Thalassiosira pseudonana* (Bacillariophyceae) provides novel insights into cell-wall synthesis processes in relation to the cell cycle. *J Phycol*. 2007;43(4):730–40.
50. Dixit S, Van Cappellen P, Bennekoum AJ. Processes controlling solubility of biogenic silica and pore water build-up of silicic acid in marine sediments. *Mar Chem*. 2001;73(3):333–52.
51. Machill S, Kohler L, Ueberlein S, Hedrich R, Kunaschk M, Paasch S, et al. Analytical studies on the incorporation of aluminium in the cell walls of the marine diatom *Stephanopyxis turris*. *Biomaterials*. 2013;26(1):141–50.
52. Lutz K, Gröger C, Sumper M, Brunner E. Biomimetic silica formation: analysis of the phosphate-induced self-assembly of polyamines. *Phys Chem Chem Phys*. 2005;7(14):2812–5.
53. Darley WM, Volcani BE. Role of Silicon in Diatom Metabolism: a Silicon Requirement for Deoxyribonucleic Acid Synthesis in the Diatom *Cylindrotheca fusiformis*. *Exp Cell Res*. 1969;58(2):334–42.
54. Kumari E, Görlich S, Poulsen N, Kröger N. Genetically programmed regioselective immobilization of enzymes in biosilica microparticles. *Adv Funct Mater*. 2020 (accepted)
55. Lucas G, Burdet P, Cantoni M, Hébert C. Multivariate statistical analysis as a tool for the segmentation of 3D spectral data. *Micron*. 2013;52–53(September–October):49–56.

Publisher's Note

Springer Nature remains neutral with regard to jurisdictional claims in published maps and institutional affiliations.